



Type Ia Supernova Distances at Redshift >1.5 from the *Hubble Space Telescope* Multi-cycle Treasury Programs: The Early Expansion Rate

Adam G. Riess^{1,2}, Steven A. Rodney³, Daniel M. Scolnic⁴, Daniel L. Shafer¹, Louis-Gregory Strolger², Henry C. Ferguson², Marc Postman², Or Graur^{5,6,22}, Dan Maoz⁷, Saurabh W. Jha⁸, Bahram Mobasher⁹, Stefano Casertano², Brian Hayden^{10,11}, Alberto Molino¹², Jens Hjorth¹³, Peter M. Garnavich¹⁴, David O. Jones¹, Robert P. Kirshner⁵, Anton M. Koekemoer², Norman A. Grogan², Gabriel Brammer², Shoubaneh Hemmati¹⁵, Mark Dickinson¹⁶, Peter M. Challis⁵, Schuyler Wolff¹, Kelsey I. Clubb¹⁷, Alexei V. Filippenko^{17,18}, Hooshang Nayyeri¹⁹, U Vivian^{9,19,23}, David C. Koo²⁰, Sandra M. Faber²⁰, Dale Kocevski²¹, Larry Bradley², and Dan Coe²

¹ Department of Physics and Astronomy, The Johns Hopkins University, 3400 North Charles Street, Baltimore, MD 21218, USA; ariess@stsci.edu

² Space Telescope Science Institute, 3700 San Martin Drive, Baltimore, MD 21218, USA

³ Department of Physics and Astronomy, University of South Carolina, 712 Main Street, Columbia, SC 29208, USA

⁴ Kavli Institute for Cosmological Physics, University of Chicago, 5640 South Ellis Avenue, Chicago, IL 60637, USA

⁵ Harvard-Smithsonian Center for Astrophysics, 60 Garden Street, Cambridge, MA 02138, USA

⁶ Department of Astrophysics, American Museum of Natural History, Central Park West and 79th Street, New York, NY 10024, USA

⁷ School of Physics and Astronomy, Tel Aviv University, Tel Aviv 69978, Israel

⁸ Department of Physics and Astronomy, Rutgers, The State University of New Jersey, Piscataway, NJ 08854, USA

⁹ Department of Physics and Astronomy, University of California, 900 University Avenue, Riverside, CA 92521, USA

¹⁰ Lawrence Berkeley National Laboratory, Berkeley, CA 94720, USA

¹¹ Department of Physics, University of California, Berkeley, CA 94720, USA

¹² Instituto de Astronomia, Geofísica e Ciências Atmosféricas, Universidade de São Paulo, Cidade Universitária, 05508-090, São Paulo, Brazil

¹³ Dark Cosmology Centre, Niels Bohr Institute, University of Copenhagen, Juliane Maries Vej 30, DK-2100 Copenhagen, Denmark

¹⁴ Department of Physics, University of Notre Dame, Notre Dame, IN 46556, USA

¹⁵ Infrared Processing and Analysis Center, California Institute of Technology, Pasadena, CA 91125, USA

¹⁶ National Optical Astronomy Observatory, 950 North Cherry Avenue, Tucson, AZ 85719, USA

¹⁷ Department of Astronomy, University of California, Berkeley, CA 94720-3411, USA

¹⁸ Miller Senior Fellow, Miller Institute for Basic Research in Science, University of California, Berkeley, CA 94720, USA

¹⁹ Department of Physics and Astronomy, University of California, Irvine, CA 92697, USA

²⁰ Department of Astronomy and Astrophysics, University of California, Santa Cruz, CA 95064, USA

²¹ Colby College, 4000 Mayflower Hill Drive, Waterville, ME 04901, USA

Received 2017 September 29; revised 2017 December 22; accepted 2018 January 4; published 2018 January 31

Abstract

We present an analysis of 15 Type Ia supernovae (SNe Ia) at redshift $z > 1$ (9 at $1.5 < z < 2.3$) recently discovered in the CANDELS and CLASH Multi-Cycle Treasury programs using WFC3 on the *Hubble Space Telescope*. We combine these SNe Ia with a new compilation of ~ 1050 SNe Ia, jointly calibrated and corrected for simulated survey biases to produce accurate distance measurements. We present unbiased constraints on the expansion rate at six redshifts in the range $0.07 < z < 1.5$ based only on this combined SN Ia sample. The added leverage of our new sample at $z > 1.5$ leads to a factor of ~ 3 improvement in the determination of the expansion rate at $z = 1.5$, reducing its uncertainty to $\sim 20\%$, a measurement of $H(z = 1.5)/H_0 = 2.69^{+0.86}_{-0.52}$. We then demonstrate that these six derived expansion rate measurements alone provide a nearly identical characterization of dark energy as the full SN sample, making them an efficient compression of the SN Ia data. The new sample of SNe Ia at $z > 1.5$ usefully distinguishes between alternative cosmological models and unmodeled evolution of the SN Ia distance indicators, placing empirical limits on the latter. Finally, employing a realistic simulation of a potential *Wide-Field Infrared Survey Telescope* SN survey observing strategy, we forecast optimistic future constraints on the expansion rate from SNe Ia.

Key words: cosmology: observations – methods: observational – supernovae: general

1. Introduction

Type Ia supernovae (SNe Ia) at redshift $z > 1$ offer unique leverage on investigations relating to the nature of their progenitors, their accuracy as distance indicators, and the parameters of the cosmological model. Unfortunately, ground-based facilities are extremely challenged to produce reliable discoveries of SNe Ia at $z > 1$, a task demanding significant and repeatable detections and robust classifications at $I \sim 26$ mag.

Thus, for the past two decades, the *Hubble Space Telescope* (HST) has offered the best perch from which to harvest these

objects, with the rate of collection limited only by its relatively modest field of view. The first robust, multi-object sample of SNe Ia at $z > 1$ came from searching the GOODS fields with the HST Advanced Camera for Surveys (ACS) and its z-band filter, with crucial near-infrared follow-up observations of the rest-frame optical light obtained using NICMOS and confirming spectroscopy from the ACS grism. The first sample of 7 SNe Ia at $z > 1.25$ provided a crucial check that dimming from astrophysical effects was not mimicking cosmic acceleration (Riess et al. 2004). A follow-up program increased the sample of reliable SNe Ia at $z > 1$ to 18 (Riess et al. 2007) followed by another 12 from targeting cluster fields (Barbary et al. 2012; Suzuki et al. 2012). This sample of ~ 30 successfully extended the SN Ia measurement of expansion

²² NSF Astronomy and Astrophysics Postdoctoral Fellow.

²³ University of California Chancellor's Postdoctoral Fellow.

to the matter-dominated era to break degeneracies between dark energy and dark matter.

Still, clues available only at $z > 1.5$ beckoned. Owing to the red-limit of *HST* CCDs and the roughly Gyr delay between progenitor formation and SN Ia explosion (Rodney et al. 2014), only ~ 3 moderately constrained SNe Ia at $z > 1.5$ were previously discovered with *HST*: SN 1997ff at $z = 1.755$, SN 2003ak at $z = 1.551$, and SCP0401 at $z = 1.713$ (Gilliland et al. 1999; Riess et al. 2001, 2004; Rubin et al. 2013). An effective program to find SNe Ia at $z > 1.5$ required WFC3-IR, the first wide-area (greater than an arcminute) infrared HgCdTe detector on *HST*, installed in 2009, which extended the red cutoff to $1.6 \mu\text{m}$. Two of the initial three Multi-Cycle Treasury (MCT) programs with WFC3, CANDELS (PI: Faber and Ferguson, Grogin et al. 2011; Koekemoer et al. 2011) and CLASH (PI: Postman, Postman et al. 2012) were selected to enable the discovery of SNe Ia at $z > 1.5$ with an additional program of coordinated SN follow-up observations (PI: Riess, Graur et al. 2014; Rodney et al. 2014). These MCT programs were three-year extragalactic imaging campaigns initiated in *HST* Cycle 18, beginning 2010 October. Both MCT programs employed ACS and WFC3-IR with cadences of ~ 50 days between epochs, chosen to match the risetime of SNe Ia time-dilated to $1.5 < z < 2.0$. (Rodney et al. 2014, hereafter R14) comprehensively described the SN search component of the CANDELS program and measured the volumetric SN Ia rate from the complete CANDELS sample of 65 SNe out to $z = 2.5$. (Graur et al. 2014, hereafter G14) presented the SN Ia rates analysis from the CLASH program, using a sample of 27 SNe detected in the *HST* parallel fields ($\sim 6'$ from the galaxy clusters that make up the primary targets for CLASH). For full details of the survey design and observations, we refer the reader to R14 and G14.

These programs together identified 15 SNe Ia at $z > 1$, 9 of which (7 at $z > 1.5$) are sufficiently well-measured to derive reliable distance estimates. Detailed studies of the first two such events were presented by Rodney et al. (2012) and Jones et al. (2013), and a novel approach to SN classification via medium-band infrared imaging was presented for two others by Rodney et al. (2015).

Here for the first time we derive a set of distance estimates for this sample calibrated for a joint cosmological analysis with a compilation of SNe Ia from previous surveys (Scolnic et al. 2017). The most significant augmentation of the extant SN Ia sample is the set of SN Ia distances presented here at $z > 1.5$, which usefully extends the SN-based determination of the expansion rate of the universe to a higher redshift, $z \approx 1.5$, than previously possible. In Section 2, we present details of the SN sample, and in Section 3, we present constraints on the scale-free expansion history and carry out some related investigations. We summarize our conclusions in Section 4.

2. SN Ia Sample

From the total set of 92 CANDELS and CLASH SNe, we have identified 15 as likely SNe Ia at $z > 1$ with sufficient confidence for use as distance indicators. We present the coordinates of these objects in Table 1, their redshifts and classifications in Table 2, the properties of their host galaxies in Table 3, and their distance-related parameters in Table 4. The light-curve photometry is given in the Appendix. For inclusion in this subset, we require at least enough samplings of the light and color curves to exceed the number of free parameters in the

light-curve fit. This effectively means that we require a minimum of four independent observation epochs, providing at least a modicum of constraint on the light-curve shape. We also require that the first epoch with $> 3\sigma$ detection must be no more than 10 days after the peak of the light curve in the rest-frame B band, consistent with the requirements used by Riess et al. (1996, 2007). Finally, we require that at least one of the epochs includes WFC3-IR observations in both the F125W and F160W bands, which provide a measurement of the SN color at rest-frame optical wavelengths for $1 < z < 2.5$.

For the cosmological analysis presented here, we further subdivide this sample into three confidence categories: *gold*, *silver*, and *bronze*, following the convention of Strolger et al. (2004), Riess et al. (2004, 2007). The gold sample comprises those SNe with compelling classifications as Type Ia, while the silver label indicates a “very likely” Type Ia classification, and the bronze objects are those that are probably Type Ia, but have some nonnegligible probability of misclassification.

As detailed by R14 and G14, the classifications of these SNe at $z > 1$ sometimes rely on photometric evidence. Spectra are available for 6 of the 15 SNe Ia at $z > 1$ (3 at $z > 1.5$), while two others use medium bands to measure the strength of SN Ia spectral features. This mixture of classification methods is necessitated by the difficulty of achieving a purely spectroscopic classification for such high-redshift SNe (see, e.g., Frederiksen et al. 2012; Rodney et al. 2012; Jones et al. 2013; Rubin et al. 2013). Photometric classification of these SNe was performed using STARDUST,²⁴ a Bayesian algorithm employing a comparison of multi-band light curves against 43 template-based models representing Type Ia and core-collapse SNe (R14). For inclusion in the gold and silver samples, we require a Type Ia classification probability $P(\text{Ia}) > 0.99$; the two objects with $0.9 < P(\text{Ia}) < 0.99$ were relegated to the bronze sample.

The gold objects are further distinguished by having at least one piece of corroborating evidence to support the Type Ia classification. For 6 objects, we have a spectroscopic observation that is well-matched by a SN Ia spectral template, presented by R14 and G14. Two more SNe have medium-band infrared imaging that provides evidence for Type Ia spectral features in medium-band minus broad-band pseudo-colors (Rodney et al. 2015). Finally, three of the gold sample SNe have a host galaxy that is classified as “early type” based on morphology and colors, indicating an old stellar population that would be unlikely to host a core-collapse SN (Riess et al. 2001).

We discard the 2 bronze SNe whose classification is too uncertain and proceed with the analysis of the remaining 13 gold and silver SNe at $z > 1$ (8 at $z > 1.5$) from the CANDELS and CLASH programs. Assuming the 3 silver SNe in the sample are Type Ia with 99% confidence, there is a $\sim 97\%$ chance that all of the SNe in the cosmological analysis are Type Ia. We combine this set (hereafter, the MCT set) with a uniformly calibrated compilation of ~ 1050 spectroscopically classified SNe Ia, the Pantheon compilation (Scolnic et al. 2017). This compilation includes SNe from the Harvard-Smithsonian Center for Astrophysics SN surveys (CfA, Hicken et al. 2009), the Carnegie Supernova Project (CSP, Stritzinger et al. 2011), the Sloan Digital Sky Survey (SDSS, Kessler et al. 2009), the Pan-STARRS1 Medium-Deep Survey (PS1, Rest

²⁴ STARDUST: Supernova Taxonomy And Redshift Determination Using SNANA Templates.

Table 1
SNe Ia from CANDELS + CLASH at $z > 1$

SN ID	Nickname	Survey	Field	α (J2000)	δ (J2000)
CLA10Cal	Caligula	CLASH	Abell 383 IR par	02:48:25.74	−03:33:08.8
CLF11Ves	Vespasian	CLASH	MACS2129 ACS par	21:29:42.60	−07:41:47.7
CLH11Tra	Trajan	CLASH	MS2137 ACS par	21:39:46.05	−23:38:34.8
CLP12Get	Geta	CLASH	RXJ2129 IR par	21:29:23.89	+00:08:24.8
COS12Car	Carter	CANDELS	COSMOS	10:00:14.72	+02:11:32.6
EGS11Oba	Obama	CANDELS	EGS	14:20:32.66	+53:02:48.2
EGS13Rut	Rutledge	CANDELS	EGS	14:20:48.11	+53:04:22.1
GND12Col	Colfax	CANDELS	GOODS-N Deep	12:36:37.58	+62:18:33.1
GND13Cam	Camille	CANDELS	GOODS-N Deep	12:37:07.37	+62:10:26.9
GND13Gar	Garner	CANDELS	GOODS-N Deep	12:36:40.81	+62:11:14.2
GND13Jay	Jay	CANDELS	GOODS-N Deep	12:36:41.38	+62:11:30.1
GND13Sto	Stone	CANDELS	GOODS-N Deep	12:37:16.77	+62:16:41.4
GSD10Pri	Primo	CANDELS	GOODS-S Deep	03:32:38.01	−27:46:39.1
GSD11Was	Washington	CANDELS	GOODS-S Deep	03:32:20.85	−27:49:41.5
UDS10Wil	Wilson	CANDELS	UDS	02:17:46.33	−05:15:24.0

et al. 2014), and the Canada–France–Hawaii Telescope Supernova Legacy Survey (SNLS, Conley et al. 2011). The compilation includes all SNe from the Rest et al. (2014) sample and from the samples included in the joint light-curve analysis (JLA; Betoule et al. 2014), all uniformly calibrated as presented in the Supercal analysis (Scolnic et al. 2015). The Pantheon compilation also includes 12 equivalently high-confidence SNe Ia at $1 < z < 1.4$ from past *HST* SN surveys (see Table 5), 9 from Riess et al. (2004) and Riess et al. (2007) and 3 from Suzuki et al. (2012), that meet the criteria given in Scolnic et al. (2017).

3. High-redshift Measurements of the Hubble Parameter

At $z \gtrsim 1$, dark energy is a small contribution to the energy budget ($\rho_\Lambda/\rho \approx 0.2$ at $z = 1$ and ≈ 0.1 at $z = 1.5$) and therefore has a small effect on dynamics. With abundant and better-measured SNe at lower redshifts, constraints on typical one-or-two-parameter dark energy models are only weakly improved by observations of SNe at $z > 1$ (see also Andersen & Hjorth 2017, regarding $z > 2$). This is especially true for combined constraints when precise distances from cosmic microwave background (CMB) and baryon acoustic oscillations (BAO) measurements are included.

Nevertheless, the new SNe at $z > 1.5$ presented here allow us to constrain the (dimensionless) Hubble parameter $E(z) \equiv H(z)/H_0$ at greater redshifts than previously possible. The quantity $H(z)$ is particularly useful because it is both a direct probe of cosmology and still closely tied to the data. As a dynamical quantity, $H(z)$ contains information about the expansion history without reference to any physical cosmological model. Also, at least for current SN Ia data, the inferred $H(z)$ measurements are fairly local; that is, they are predominantly influenced by SNe at nearby redshifts. The quantity $E(z)$, which contains similarly useful information but can be measured using SN Ia data alone, makes the results independent of uncertainties associated with the determination of the absolute distance scale of SNe Ia (Riess et al. 2016).

As a direct probe of the expansion rate ($H \equiv \dot{a}/a$), measurements of $E(z)$ are particularly dense with cosmological information. They provide, for instance, a straightforward way to test or falsify a given cosmological model (Mortonson et al. 2009, 2010; Shafieloo & Clarkson 2010). Given current constraints on its parameters, the flat Λ CDM model already

makes very precise predictions for such basic observables. Constraints on the matter density Ω_m from combined probes (e.g., Ade et al. 2016) imply that $E(z)$, defined to be exactly one at $z = 0$, is predicted to a precision ranging from $\sim 0.1\%$ at $z = 0.1$ to $\sim 1\%$ at $z = 2$. Therefore, any new, independent measurement of $E(z)$, particularly in a new redshift range, is a direct and nontrivial test of the standard cosmological model. Given the present $>3\sigma$ tension between $H(z)$ calibrated at $z \approx 0$ (Riess et al. 2016) and at $z \approx 1100$ by the CMB (Ade et al. 2016), it is especially worthwhile to see if the expansion rate fails to match the standard Λ CDM model prediction anywhere along this redshift range.

Furthermore, as we will illustrate, accurate estimates of $E(z)$ from SN Ia data are a convenient and efficient form of data compression, allowing one to obtain SN Ia constraints on dark energy and other cosmological parameters quickly and robustly using a very small and easily provided set of measurements. Such data compression techniques will be especially useful as SN Ia samples grow significantly in size in the coming decade. Some recent SN Ia analyses (e.g., Betoule et al. 2014) have included compressed versions of the SN data in the form of binned distance moduli, and it is worth investigating the extent to which $E(z)$ measurements can serve a similar purpose.

Finally, quantifying SN Ia constraints on $E(z)$ facilitates a more direct comparison with other cosmological probes of geometry, such as anisotropic fits of the BAO feature, which effectively constrain a dimensionless measure of the expansion rate, the product of the Hubble parameter and the sound horizon, where the latter is inferred precisely from CMB observations.

Our aim here is to employ a new, well-calibrated compilation of SNe Ia, featuring the final addition of 9 new SNe Ia at $z > 1$ from the CANDELS and CLASH programs, to obtain unbiased estimates of the Hubble parameter $E(z)$ up to $z \approx 1.5$.

In what follows, we will briefly review some proposed methodologies for inferring $E(z)$ from SN Ia data (Section 3.1) and then discuss our approach and how it overcomes some important limitations (Section 3.2). In Section 3.3, we present constraints on $E(z)$ for the Pantheon SN compilation supplemented by the MCT SNe (i.e., Pantheon + MCT²⁵). We illustrate how the handful of high-redshift SNe from

²⁵ Note that the Pantheon compilation as defined in Scolnic et al. (2017) includes the MCT SNe presented here.

Table 2
Final Redshifts and Classifications

SN ID	Redshift ^a	Redshift Source ^b	$P(\text{Ia})^c$	Supporting Evidence ^d	Confidence ^e	Primary Reference ^f
CLA10Cal	1.800 ± 0.1	phot- z	0.95	...	bronze	Graur et al. (2014)
CLF11Ves	1.206 ± 0.007	spec- z (<i>HST</i> +G800L)	>0.99	spec, early-type host	gold	Graur et al. (2014)
CLH11Tra	1.520 ± 0.04^g	phot- z	>0.99	early-type host	gold	Graur et al. (2014)
CLP12Get	1.700 ± 0.04	phot- z	>0.99	early-type host	gold	Graur et al. (2014)
COS12Car	1.540 ± 0.04	SN spec- z (<i>HST</i> +G141)	>0.99	spec	gold	Rodney et al. (2014)
EGS11Oba	1.409 ± 0.002	spec- z (Keck+LRIS,DEIMOS)	0.9	...	bronze	Rodney et al. (2014)
EGS13Rut	1.614 ± 0.005	spec- z (<i>HST</i> +G141, single line)	>0.99	...	silver	Rodney et al. (2014)
GND12Col	$2.260^{+0.02}_{-0.10}$	phot- z	>0.99	med. band	gold	Rodney et al. (2015)
GND13Cam	1.222 ± 0.002	spec- z (AGHAST, <i>HST</i> +G141)	>0.99	...	silver	Rodney et al. (2014)
GND13Gar	1.070 ± 0.02	SN spec- z (<i>HST</i> +G800L)	>0.99	spec	gold	Rodney et al. (2014)
GND13Jay	1.030 ± 0.01	spec- z (AGHAST, <i>HST</i> +G141)	>0.99	...	silver	Rodney et al. (2014)
GND13Sto	1.800 ± 0.02	spec- z	>0.99	med. band	gold	Rodney et al. (2015)
GSD10Pri	1.550 ± 0.0001	spec- z	>0.99	spec	gold	Rodney et al. (2012)
GSD11Was	1.330 ± 0.02	spec- z (<i>HST</i> +G141)	>0.99	spec	gold	Rodney et al. (2014)
UDS10Wil	1.914 ± 0.001	spec- z	>0.99	spec	gold	Jones et al. (2013)

Notes.

^a Final composite redshift, incorporating all evidence from SN and host.

^b All phot- z and spec- z redshifts are principally constrained by the host galaxy, except where a SN spec- z is noted.

^c Classification probability from the SN light curve, including host redshift priors, using STARDUST (R14).

^d Additional factors influencing the classification confidence. “spec”: SN spectrum; “med. band”: pseudocolors from medium-band infrared imaging; “early-type host”: host galaxy is identified as an early-type galaxy, unlikely to host core-collapse SNe.

^e Confidence in the Type Ia SN classification.

^f Primary reference for further information on discovery, redshift, and classification.

^g Revised from Graur et al. (2014).

CANDELS and CLASH significantly improves the determination of $E(z)$ at $z \approx 1.5$. We also illustrate the effectiveness of the $E(z)$ measurements in subsequent inference of cosmological parameters, and, in Section 3.4, the ability of the high-redshift SNe Ia to distinguish cosmology from SN Ia evolution. Finally, employing a realistic simulation of a potential *Wide-Field Infrared Survey Telescope* (WFIRST) SN survey observing strategy, we compare our current results with optimistic future constraints on $E(z)$ (Section 3.5).

3.1. SN Ia Measurements of $E(z)$

SNe Ia measure distances most directly; roughly speaking, each SN provides an independent measurement of the luminosity distance to its redshift. For a flat universe, we have

$$d_L(z) = \frac{c}{H_0}(1+z) \int_0^z \frac{dz'}{E(z')}; \quad (1)$$

therefore the (inverse) Hubble parameter, the derivative of the comoving distance, must be inferred indirectly when starting from raw SN Ia data.

A variety of interrelated methods have been used for this purpose. Some analyses have focused on model-independent reconstruction of an analytical $E(z)$ function or of other dynamical quantities like the deceleration parameter $q(z)$ (Sahni & Starobinsky 2006; Shafieloo et al. 2006; Shafieloo 2007; Ishida & de Souza 2011). Such reconstructions are useful for understanding where the data are most constraining, and they can indicate whether the functional form for $H(z)$ naturally preferred by the data is consistent with that of a physical model like Λ CDM. On the other hand, it is not possible, or at least not straightforward, to subsequently incorporate the reconstructions in a likelihood function, or otherwise in a statistical analysis, in order to constrain cosmological parameters.

Other methods focus on obtaining direct measurements of $E(z)$ at several redshifts by smoothing and/or weighting the individual SNe and differentiating the distance-redshift relation (Tegmark 2002; Daly & Djorgovski 2003, 2004; Daly et al. 2008). One proposed method (Wang & Tegmark 2005), which has been employed in some subsequent analyses (Riess et al. 2007; Avgoustidis et al. 2009; Mortsell & Clarkson 2009), seeks direct, independent estimates of $E(z)$ in redshift bins by first converting SN distance moduli into their corresponding comoving distances r_i , then transforming these r_i into noisy, but locally unbiased, estimates of $E(z)^{-1}$ between neighboring SNe. A specific weighted average then yields a minimum-variance estimate of $E(z)^{-1}$ over a wider redshift bin. We have verified numerically²⁶ that this procedure is actually *equivalent* to the familiar weighted least-squares fit of a line to the r_i versus z_i data over the same wide redshift bin, where the slope corresponds to $E(z)^{-1}$. Both the least-squares estimator and that of Wang & Tegmark (2005) have been shown to be unbiased and have minimum variance, assuming SN redshifts are known exactly and $E(z)$ is constant over the redshift bin, so it is not surprising that these estimators coincide.

While such an approach is attractive in that it directly transforms the SN distances into independent measurements of $E(z)$ at different redshifts, it has notable problems that make it unsuitable in practice. The first step requires converting SN distance moduli into comoving distances, and one must therefore assume a value for the intercept of the Hubble diagram, which is unknown a priori. As this quantity is partially degenerate with $E(z)$, particularly the lowest-redshift measurement, fixing the intercept to some best-fit value would

²⁶ Proving this analytically involves calculating the inverse of a symmetric tridiagonal matrix (the covariance matrix describing the individual noisy estimates of the slope). We were able to verify analytically for the simplified case of a fit over a bin with 3 SNe with equal distance uncertainties.

Table 3
SN Host Galaxy Data

SN ID	Host α (J2000)	Host δ (J2000)	Host Redshift ^a	Morphology	Star Formation	Redshift Source
CLA10Cal	02:48:25.74	−03:33:08.8	1.8 ± 0.1	spheroid/disk	active	phot-z
CLF11Ves	21:29:42.62	−07:41:47.5	1.206 ± 0.007	spheroid	passive	<i>HST</i> +ACS
CLH11Tra	21:39:46.04	−23:38:34.6	1.52 ± 0.04	spheroid	passive	phot-z
CLP12Get	21:29:23.92	+00:08:23.8	1.70 ± 0.04	spheroid	passive	phot-z
COS12Car ^b	10:00:14.72	+02:11:32.6	...	undetected	undetected	...
EGS11Oba	14:20:32.67	+53:02:48.1	1.409 ± 0.002	disk/irregular	active	Keck+LRIS
EGS13Rut	14:20:48.11	+53:04:22.1	1.614 ± 0.005	disk	active	<i>HST</i> +WFC3
GND12Col	12:36:37.51	+62:18:32.6	$2.260^{+0.02}_{-0.10}$	spheroid	active	phot-z
GND13Cam	12:37:07.38	+62:10:27.2	1.222 ± 0.002	spheroid/disk	starburst	<i>HST</i> +WFC3
GND13Gar	12:36:40.80	+62:11:14.6	1.86 ± 0.77	undefined	starburst	phot-z
GND13Jay	12:36:41.37	+62:11:29.5	1.03 ± 0.01	disk	active	<i>HST</i> +WFC3
GND13Sto	02:37:16.59	+62:16:43.4	1.80 ± 0.02	undefined	active	phot-z
GSD10Pri	03:32:37.99	−27:46:38.7	1.550 ± 0.0001	irregular	starburst	VLT+X-Shooter
GSD11Was	03:32:20.86	−27:49:41.5	1.042 ± 0.23	disk	starburst	<i>HST</i> +WFC3
UDS10Wil	02:17:46.33	−05:15:23.9	1.914 ± 0.001	spheroid	starburst	VLT+X-Shooter

Notes.

^a Photometric redshifts are marked as “phot-z” and spectroscopic redshifts are labeled with the observatory and instrument employed.

^b No plausible host galaxy was identified for SN COS12Car. The coordinates given are for the SN itself.

artificially remove a degree of freedom from the fit, resulting in underestimated uncertainties. One could instead interpret the estimates as estimates of $AE(z)^{-1}$, where A is an arbitrary constant. In this case, though, properly extracting cosmological information from the $E(z)$ measurements would require fully marginalizing over A in a fit to multiple measurements of $AE(z)^{-1}$.

Furthermore, an $E(z)$ estimate using this method reflects some average of $E(z)$ over the redshift bin, not necessarily the value at the bin’s center. Unless $E(z)$ is constant over the redshift bin, this will lead to a bias, and since only a handful of $E(z)$ values can be constrained robustly with current data, one might expect the bias to be significant. Indeed, by simulating instances of our SN data (see Section 3.2), we have verified that biases in such $E(z)$ estimates are typically a large fraction (~ 0.5) of their uncertainty, making the measurements unsuitable for later cosmological inference.

3.2. Parametrized $E(z)$ and Interpolation

We now describe a somewhat different approach for determining $E(z)$ from SN Ia data. We explain how it avoids the problems discussed in Section 3.1 and provides more meaningful and robust $E(z)$ measurements. We will assume that the true, underlying $E(z)$ function is a continuous, smooth function of redshift, which is certainly the case for most physical and empirical models studied in the literature.

In our approach, we parametrize $E(z)$ by its value at several specific redshifts and employ a basic interpolation scheme to define the complete $E(z)$ function, which can then be numerically integrated to compute the luminosity distance and compare to the data. This allows us to constrain the $E(z)$ parameters using the full SN data set in its raw form, as one would in a standard dark energy analysis. This way, any nuisance parameters associated with the SN data, notably the distance scale or Hubble diagram intercept, can be properly marginalized over in the fit.

While the total number of $E(z)$ values to constrain is somewhat arbitrary, there are several considerations. Choosing too many $E(z)$ parameters results in weaker constraints and

posterior distributions that are less likely to be Gaussian. Choosing too few $E(z)$ values increases the chance that the estimates will be biased, as the interpolating function will deviate from the functional form of the underlying cosmology. The specific redshifts, while also somewhat arbitrary, should reflect the redshift range and distribution of the SNe. Since the $E(z)$ measurements, especially those at neighboring redshifts, will naturally be somewhat correlated, choosing too small a separation in redshift between a given pair will lead to undesirably large pairwise correlations in the estimates. We choose redshifts such that the resulting $E(z)$ correlation coefficients are $\lesssim 0.5$ to avoid such redundancy.

Overall, we find that employing a shape-preserving piecewise-cubic Hermite interpolating polynomial (implemented as `pchip` in MATLAB; see Kahaner et al. 1988) to interpolate (and extrapolate) the $E(z)$ function works particularly well, though other interpolation schemes (various splines, simple linear interpolation) are also generally suitable. For any specified $E(z)$ (any fiducial cosmology), it is straightforward to determine whether the $E(z)$ estimates resulting from the interpolation and fitting procedure are unbiased. To check this, we repeatedly simulate instances of our SN Ia data; that is, we keep the same SN redshifts and covariance matrix as the real SN data, but repeatedly sample the distance moduli from a multivariate Gaussian centered on the fiducial cosmology. Of course, unbiased constraints for the fiducial cosmology do not guarantee unbiased results for other cosmologies. In principle, one could perform this check for each specific model of interest; however, there is reason to worry only when a model predicts $E(z)$ to vary rapidly or have features too narrow to be captured by the widely spaced $E(z)$ parameters. For the highest-redshift SNe Ia, a modest amount ($\sim 25\%$) of the integral of $E(z)^{-1}$ must be evaluated via extrapolation beyond the last redshift anchor of the $E(z)$ function. However, our simulations indicate that this does not bias this highest-redshift measurement of $E(z)$. Indeed, we have verified that all of the $E(z)$ measurements are biased by $\lesssim 10\%$ of their individual statistical uncertainties.

In essence, our procedure trades the ability to make direct, independent measurements of $E(z)$ at redshifts that are somewhat uncertain (and not randomly so) for the ability to

Table 4
SALT2 Light-curve Fit Parameters

SN ID	m_B	x_1	c	Δ_B	$\mu(\text{mag})$	Notes
CLA10Cal	poor light-curve fit
CLF11Ves	25.38 (0.091)	-1.24 (0.60)	-0.288 (0.101)	+0.27	25.73 (0.34)	
CLH11Tra	25.30 (0.095)	-3.35 (2.10)	-0.272 (0.090)	fails x_1 cut ($x_1 < -3$, $\sigma_{x_1} > 1$)
CLP12Get	25.73 (0.088)	+1.01 (0.95)	-0.139 (0.098)	+0.18	26.06 (0.28)	
COS12Car	26.14 (0.122)	+2.35 (0.83)	+0.152 (0.083)	+0.07	25.91 (0.21)	
EGS11Oba	poor light-curve fit
EGS13Rut	25.92 (0.071)	+0.98 (1.08)	+0.055 (0.046)	-0.07	25.93 (0.20)	
GND12Col	26.81 (0.056)	+0.02 (0.91)	+0.128 (0.133)	-0.50	26.88 (0.25)	
GND13Cam	25.91 (0.061)	-1.35 (0.48)	-0.083 (0.043)	Hubble diagram outlier ($>4\sigma$)
GND13Gar	25.42 (0.259)	+0.02 (0.99)	+0.310 (0.179)	fails color cut ($c > 0.3$)
GND13Jay	24.56 (0.672)	-2.04 (0.92)	-0.373 (0.447)	fails color cut ($c < -0.3$)
GND13Sto	26.15 (0.074)	-0.48 (0.70)	+0.000 (0.071)	-0.17	26.20 (0.19)	
GSD10Pri	25.76 (0.089)	-0.51 (0.41)	-0.186 (0.078)	+0.16	26.01 (0.19)	
GSD11Was	25.32 (0.057)	+1.04 (0.67)	-0.089 (0.039)	+0.09	25.60 (0.15)	
UDS10Wil	26.28 (0.172)	-1.64 (0.76)	+0.082 (0.152)	-0.43	26.15 (0.26)	

obtain precise, unbiased $E(z)$ estimates at specific redshifts. Only this latter type of estimate allows for accurate subsequent cosmological inference with the $E(z)$.

3.3. SN Ia Constraints on $E(z)$

We now constrain $E(z)$ for the Pantheon compilation of 1040 SNe Ia, which we will supplement with the high-redshift CANDELS and CLASH SNe. The Pantheon compilation (Scolnic et al. 2017) includes data from multiple surveys (CfA(1–4), CSP, SDSS, SNLS, Pan-STARRS1, *HST*) calibrated for a joint cosmological analysis. Below we summarize the key aspects of the Pantheon analysis, and we refer the reader to Scolnic et al. (2017) for additional details and a complete discussion.

The Pantheon analysis presents the full set of spectroscopically confirmed SNe Ia from the Pan-STARRS1 (PS1) Medium Deep Survey, building on the earlier analysis of the first 1.5 yr of PS1 (Rest et al. 2014; Scolnic et al. 2014). It relies on the Supercal cross-calibration procedure presented by Scolnic et al. (2015), which uses the relative consistency of the Pan-STARRS1 photometry over 3π steradians of the sky to tie together the photometric systems of the individual surveys. The Pantheon analysis also incorporates the BBC methodology of Kessler & Scolnic (2017) (see also Scolnic & Kessler 2016), which corrects for distance biases dependent on the light-curve properties of the SNe and the surveys from which they are selected.

The Pantheon analysis employs the SALT2 light-curve fitter (Guy et al. 2007; Betoule et al. 2014), which determines an overall normalization of the log-flux (m_B), a shape parameter (x_1), and a color (c) for each SN light curve, along with associated uncertainties. We standardize the SNe by modeling an individual SN Ia distance modulus as

$$\mu = m_B - M + \alpha x_1 - \beta c + \Delta_M + \Delta_B. \quad (2)$$

The Δ_M term is an additional correction for the empirical host-mass step, where SNe in high-stellar-mass host galaxies ($\log_{10}(M_*/M_\odot) \gtrsim 10$) are ~ 0.05 mag brighter on average, after light-curve standardization.²⁷ The Δ_B term represents the

²⁷ It is difficult to estimate the masses of high-redshift hosts in a way that is consistent with lower-redshift estimates. Therefore, in the analysis, the MCT SNe were assumed to be in low-mass hosts but near the host-mass cut such that a systematic uncertainty estimated by shifting the mass cut effectively marginalizes over their unknown host masses.

distance bias correction. Note that M , α , β , and the amplitude of the mass step (included in the Δ_M term) are all nuisance parameters that must be determined by a fit to the data. In our analysis, only M (effectively, the Hubble diagram offset) is fit along with the cosmological parameters $E(z)$. The other parameters are well determined independently of cosmology in the Pantheon analysis. The inferred values are $\alpha \approx 0.15$ – 0.16 and $\beta \approx 3.0$ – 3.7 , where the results vary depending on the intrinsic scatter model.²⁸ Finally, note that the distance modulus as predicted by the cosmological model is given by

$$\mu(z) = 5 \log_{10} \left[\frac{d_L(z, \mathbf{p})}{1 \text{ Mpc}} \right] + 25, \quad (3)$$

where d_L is the luminosity distance, which is a function of redshift and also depends on the set of cosmological parameters \mathbf{p} .

The statistical uncertainties of SN distance moduli are modeled, in the standard way, as a combination of observational measurement uncertainty, intrinsic scatter, and additional scatter due to gravitational lensing, peculiar velocities, and redshift measurement uncertainty.²⁹ The inferred value for the intrinsic scatter is $\sigma_{\text{int}} \approx 0.1$, although, like α and β , the value depends on the intrinsic scatter model. After bulk-flow corrections are applied to the low-redshift SNe, we add a peculiar-velocity scatter of $\sigma_v = 250 \text{ km s}^{-1}$. We assume a value $\sigma_{\text{lens}} = 0.055z$ for the lensing scatter (Jönsson et al. 2010). Note that the distribution of the shift in observed magnitude due to lensing is non-Gaussian (e.g., Jönsson et al. 2006), with a tail of strongly magnified SNe; however, by examination of foreground structures we have verified that none of our CANDELS or CLASH SNe are likely to fall in this tail, making the lensing scatter contribution to the distance uncertainty a good approximation. Note that there

²⁸ In the Pantheon analysis, two alternative models for the intrinsic scatter are separately used to derive distance bias corrections, which are then averaged, with half of the difference included in the systematic uncertainty budget.

²⁹ Separate from standard propagation of redshift uncertainty, the derived distance moduli themselves depend on the observed redshift. We have verified that, for SN GND12Col, which has a large redshift uncertainty with asymmetric errors, repeating the analysis with both its redshift and distance shifted by 1σ does not significantly affect the results.

Table 5
SNe Ia at $z > 1$ from Other Surveys

SN ID	Nickname	Survey ^a	Confidence ^b	Redshift	References
1997ff	1997ff	HDFN	Gold	1.755	Riess et al. (2001)
2002fw	Aphrodite	Higher- z GOODS	Gold	1.30	Riess et al. (2004)
2002fx	Athena	Higher- z GOODS	Silver	1.40	Riess et al. (2004)
2002hp	Thoth	Higher- z GOODS	Gold	1.305	Riess et al. (2004)
2002ki	Nanna	Higher- z GOODS	Gold	1.141	Riess et al. (2004)
2003aj	Inanna	Higher- z GOODS	Silver	1.307	Riess et al. (2004)
2003ak	Gilgamesh	Higher- z GOODS	Silver	1.551	Riess et al. (2004)
2003az	Torgasak	Higher- z GOODS	Silver	1.265	Riess et al. (2004)
2003dy	Borg	Higher- z GOODS	Gold	1.34	Riess et al. (2004)
HST04Eag	Eagle	Higher- z PANS	Gold	1.019	Riess et al. (2007)
HST04Gre	Greenburg	Higher- z PANS	Gold	1.14	Riess et al. (2007)
HST04Mcg	Mcguire	Higher- z PANS	Gold	1.357	Riess et al. (2007)
HST04Sas	Sasquatch	Higher- z PANS	Gold	1.39	Riess et al. (2007)
HST05Fer	Ferguson	Higher- z PANS	Gold	1.02	Riess et al. (2007)
HST05Gab	Gabi	Higher- z PANS	Gold	1.12	Riess et al. (2007)
HST05Koe	Koekemoer	Higher- z PANS	Gold	1.23	Riess et al. (2007)
HST05Lan	Lancaster	Higher- z PANS	Gold	1.235	Riess et al. (2007)
HST05Str	Strolger	Higher- z PANS	Gold	1.027	Riess et al. (2007)
SCP0401	SCP0401	SCP GOODS	Gold	1.713	Rubin et al. (2013)
SCP05D0	Frida	SCP CSS	Gold	1.014	Suzuki et al. (2012)
SCP05D6	Maggie	SCP CSS	Gold	1.315	Suzuki et al. (2012)
SCP06A4	Aki	SCP CSS	Silver	1.192	Suzuki et al. (2012)
SCP06C0	Noa	SCP CSS	Gold	1.092	Suzuki et al. (2012)
SCP06F12	Caleb	SCP CSS	Silver	1.110	Suzuki et al. (2012)
SCP06G4	Shaya	SCP CSS	Gold	1.35	Suzuki et al. (2012)
SCP06H5	Emma	SCP CSS	Gold	1.231	Suzuki et al. (2012)
SCP06K0	Tomo	SCP CSS	Gold	1.415	Suzuki et al. (2012)
SCP06K18	Alexander	SCP CSS	Silver	1.411	Suzuki et al. (2012)
SCP06N33	Naima	SCP CSS	Silver	1.188	Suzuki et al. (2012)
SCP06R12	Jennie	SCP CSS	Gold	1.212	Suzuki et al. (2012)
SCP06U4	Julia	SCP CSS	Gold	1.05	Suzuki et al. (2012)

Notes.

^a *HDFN*: SN 1997ff was discovered in observations of the Hubble Deep Field North (HDFN; Gilliland et al. 1999; Dickinson et al. 2001). *Higher- z GOODS/PANS*: Discoveries by the Hubble Higher- z SN Search team, from the SN component of the Great Observatories Origins Deep Survey (GOODS, *HST*-GO-9728, *HST*-GO-9352, *HST*-GO-9583; Giavalisco et al. 2004; Strolger et al. 2004) and the successor program Probing Acceleration Now with Supernova (PANS, *HST*-GO-10339; Riess et al. 2007). *SCP-GOODS/CSS*: Discoveries by the Supernova Cosmology Project (SCP) on the GOODS fields (*HST*-GO-9727) or in the Cluster Supernova Search (CSS, *HST*-GO-9425; Dawson et al. 2009).

^b Confidence in the Type Ia classification, as reported by Riess et al. (2007) or Suzuki et al. (2012), where the latter have been translated from “secure/probable/plausible” to “gold/silver/bronze.”

is also statistical uncertainty in the host-mass correction and the distance bias correction.

The Pantheon analysis also includes a rigorous analysis of systematic errors, adding terms to the covariance matrix of SN distances to account for uncertainties in photometric calibration (including terms for individual survey calibration, the Supercal cross-calibration procedure, and the SALT2 model itself), the intrinsic scatter model, survey selection functions, Milky Way dust extinction, β evolution, the host mass step and its evolution, and peculiar velocity coherent flow corrections.

Standard data-quality cuts were applied to remove SNe that are not expected to follow the empirical standardization relations. Specifically, we keep only SNe with $|x_1| < 3$, $\sigma_{x_1} < 1$, $|c| < 0.3$, a light-curve fit with $\chi^2/N_{\text{dof}} < 3$, and an uncertainty in the time of peak brightness of less than 2 days. Similar cuts have been used in most recent SN Ia cosmological analyses (e.g., Betoule et al. 2014; Rest et al. 2014; Riess et al. 2016). These cuts eliminate 3 of the silver and gold MCT SNe (CLH11Tra, GND13Gar, GND13Jay; see Table 4).

Finally, a 4σ outlier rejection from the best-fit Hubble diagram is applied and removes GND13Cam, leaving 9 *HST* MCT SNe Ia in the joint analysis.³⁰ Note that here we do include EGS13Rut, which is on the edge of the σ_{x_1} cut but has typical light-curve fit parameters. Although the final MCT addition of 9 SNe represents $< 1\%$ of the combined sample, the unusually high redshifts (7 with $z > 1.5$) provide unique leverage on $E(z)$ at $z = 1.5$.

Following the methodology and discussion in Section 3.2, we parametrize $E(z)^{-1}$ by its value at six redshifts (chosen to best summarize the sample) and therefore have six free parameters to constrain. It is important to remember that the Hubble diagram offset is a free parameter as well, though we analytically marginalize over this offset, with a flat prior, in the likelihood. We assume a flat universe ($\Omega_k = 0$) throughout,

³⁰ In the Pantheon analysis, additional cuts were applied to remove SNe without an observation at least 5 days after peak brightness and with light-curve parameters that do not fall in the simulated distribution from the BBC method (see Scolnic et al. 2017). These cuts do not remove any of the remaining MCT SNe.

Table 6
Pantheon + MCT SN Ia Measurements of $E(z)$

z	$E(z)^{-1a}$	Correlation Matrix						$E(z)$	Distance Residual $\Delta\mu/(0.01 \text{ mag})^b$
0.07	1.007 ± 0.024	1.00						0.994 ± 0.023	-0.13 ± 0.99
0.2	0.898 ± 0.016	0.40	1.00					1.113 ± 0.020	-0.23 ± 1.26
0.35	0.893 ± 0.029	0.52	-0.13	1.00				1.122 ± 0.037	$+0.23 \pm 1.32$
0.55	0.732 ± 0.033	0.35	0.35	-0.18	1.00			1.369 ± 0.063	$+0.11 \pm 1.97$
0.9	0.652 ± 0.051	0.02	-0.08	0.19	-0.41	1.00		1.54 ± 0.12	$+1.15 \pm 2.85$
1.5	0.337 ± 0.078	0.00	-0.06	-0.05	0.16	-0.21	1.00	$2.69^{+0.86}_{-0.52}$	-3.42 ± 6.78

Notes.

^a Mean and standard deviation of the marginalized likelihood, approximately Gaussian in all cases.

^b Effective distance moduli relative to those of a fiducial Λ CDM cosmology ($\Omega_m = 0.3$), as determined by an interpolated fit to the residuals using the same redshift control points as the $E(z)$ analysis.

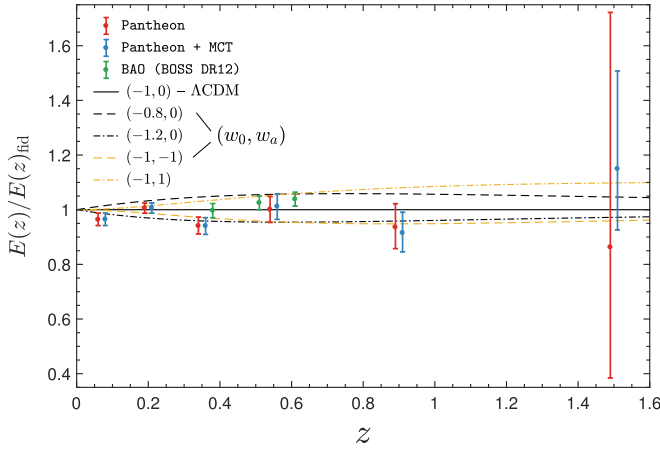


Figure 1. Constraints on $E(z) \equiv H(z)/H_0$, relative to $E(z)$ for a fiducial Λ CDM model ($\Omega_m = 0.3$). We compare the constraints with (blue points) and without (red points) the high-redshift CANDELS and CLASH (MCT) SNe Ia. Note that these $E(z)$ measurements are correlated and have non-Gaussian distributions (the error bars enclose 68.3% of the likelihood). For comparison, we also show the three (correlated) measurements of $E(z)$ from combined BOSS DR12 BAO data (Alam et al. 2017) after calibration with *Planck* Λ CDM constraints on $H_0 r_d$ (green points).

so the $E(z)$ measurements are cosmological-model-dependent in this sense. To obtain the constraints, we sample the likelihood using a custom Markov chain Monte Carlo (MCMC) code employing the basic Metropolis–Hastings algorithm. We impose flat, hard-bound priors on the $E(z)^{-1}$ parameters wide enough that extending the bounds does not affect the resulting constraints. The final MCMC chains were inspected to verify convergence.

The resulting marginalized posterior likelihoods for $E(z)^{-1}$ are Gaussian to a good approximation, and the constraints are given in Table 6. In Figure 1, we convert the measurements of $E(z)^{-1}$ into $E(z)$ measurements by reprocessing the MCMC chains and then compare the results with and without the MCT SNe. It is not surprising that the MCT SNe substantially improve the measurement of $E(z)$ at $z = 1.5$. They permit a $\sim 20\%$ measurement of $E(z = 1.5)$, roughly a factor of three improvement over the result without the MCT SNe. While the CANDELS and CLASH SNe mostly affect the measurement at $z = 1.5$, they also improve and shift some lower-redshift measurements, which are somewhat correlated ($\approx 8\%$ and 4%

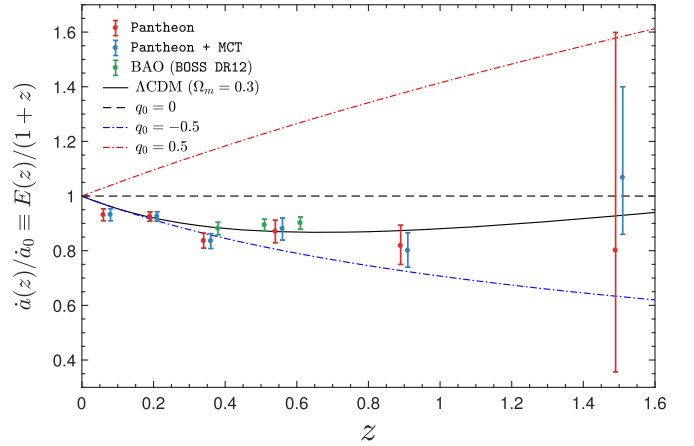


Figure 2. For the same data as in Figure 1, we show constraints on the time derivative of the scale factor $\dot{a}(z)$ relative to its present value, obtained by scaling the $E(z)$ values by $(1+z)^{-1}$. We compare the fiducial Λ CDM model to alternative models with a constant deceleration parameter $q_0 = 0$ (coasting cosmology), $q_0 = -0.5$ (pure acceleration), and $q_0 = 0.5$ (pure deceleration), all assuming a flat universe.

improvements at $z = 0.9$ and 0.55 , respectively). By eye, the set of $E(z)$ measurements may appear somewhat discrepant with the fiducial Λ CDM model, but the overall χ^2 , which includes the moderate correlations, is 6.7 for the 6 degrees of freedom.

In Figure 2, we scale $E(z)$ by $(1+z)^{-1}$ to illustrate the constraints on the time derivative of the scale factor $\dot{a}(z)$, relative to its present value, for the same data shown in Figure 1. In this space, it is clear that the low-redshift and high-redshift $E(z)$ measurements together provide evidence for both recent acceleration and earlier deceleration epochs, as predicted by standard cosmological models. In addition to the fiducial Λ CDM model, we show dynamical models with fixed deceleration parameter q_0 . The $\dot{a}(z)$ values track the $q_0 = -0.5$ model at $z \lesssim 0.5$ (where the low- z behavior matches that of a Λ CDM model with $\Omega_m \approx 0.3$) but show deceleration with respect to that curve at higher redshifts. The coasting cosmology ($q_0 = 0$), pure acceleration cosmology ($q_0 = -0.5$), and pure deceleration cosmology ($q_0 = 0.5$, equivalent to a flat CDM model with $\Omega_m = 1$) are strongly disfavored with $\Delta\chi^2 = 78.9$, $\Delta\chi^2 = 40.5$, and $\Delta\chi^2 = 357.9$, respectively, for 6 degrees of freedom. The measurement at

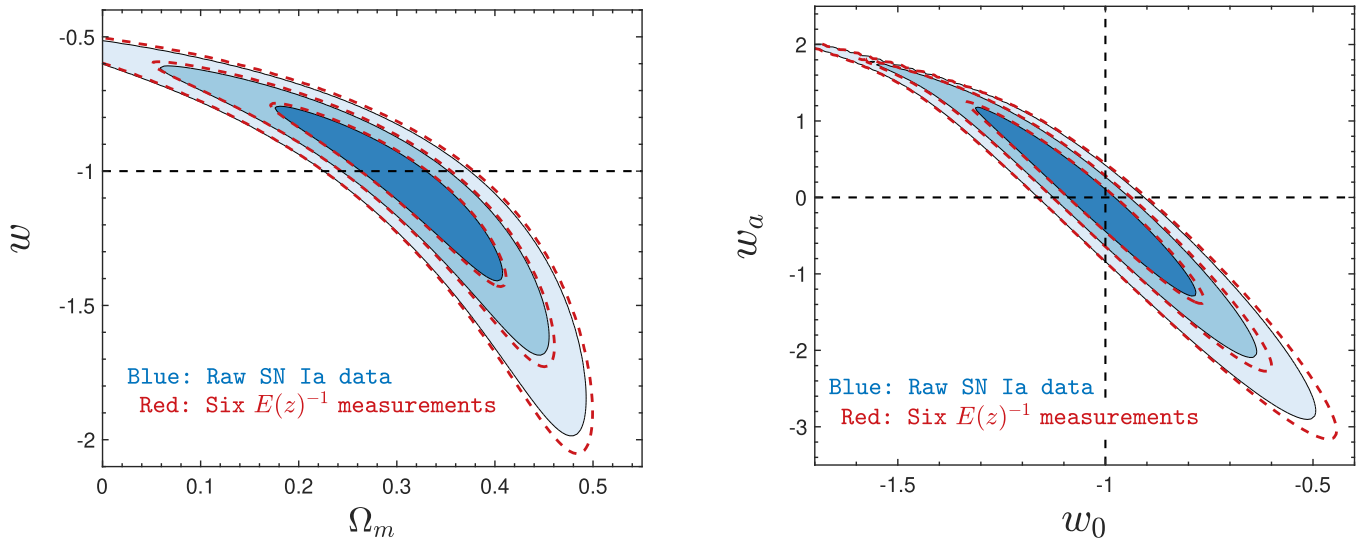


Figure 3. Constraints on Ω_m and a constant equation-of-state parameter w in a flat universe (left panel) and for the w_0 - w_a model (Chevallier & Polarski 2001; Linder 2003), marginalized over Ω_m and also assuming a flat universe (right panel). We compare the constraints when using the full SN Ia likelihood with individual distance moduli (filled blue contours) with the constraints from the six moderately correlated $E(z)$ measurements (open red contours). Contours contain 68.3%, 95.4%, and 99.7% of the likelihood, and for the w_0 - w_a constraints we have also included distance priors derived from *Planck* data (Ade et al. 2016).

$z = 1.5$ alone, while consistent with the other models, disfavors $q_0 = -0.5$ with $\Delta\chi^2 = 14.2$.

As an illustration of the power of the $E(z)$ measurements in constraining (spatially flat) cosmologies, we compare constraints on common dark energy parameterizations in Figure 3. Remarkably, the constraints are nearly identical whether the parameters are constrained with the SN Ia data directly or with the $E(z)$ measurements in Table 6. It may not be too surprising that $E(z)$ captures the constraining power of the SNe for simple one-or-two-parameter models. One would not expect the same for fits with many degrees of freedom (e.g., more complicated dark energy models); in practice, however, current and near-future SN Ia data can only meaningfully constrain 2–3 expansion parameters anyway. For models that assume a flat universe and predict fairly smooth, featureless $H(z)$, the $E(z)$ constraints will be an efficient summary of the present SN Ia data.

3.4. High-redshift SNe Ia and Evolution

The use of SNe Ia as standardizable candles across redshift relies on the understanding that their uncommonly homogeneous luminosities and colors follow from their nature as carbon–oxygen white dwarfs close to the Chandrasekhar mass. While uncertainty persists regarding *how* these degenerate stars approach that mass limit, either by accretion from a nondegenerate companion or through the tidal disruption followed by accretion of a degenerate companion, there has long been agreement about this model based on the well-understood physics of degenerate stars (Hoyle & Fowler 1960; Arnett 1969; Colgate & McKee 1969). The thermonuclear detonation of a Chandrasekhar-mass carbon–oxygen white dwarf yields a mass of radioactive nickel whose energy output matches that of a SN Ia (Arnett et al. 1985) and whose modeled nucleosynthesis matches its spectral elements (Nomoto et al. 1984). More recently, predisccovery observations of SN 2011fe, a prototypical

SN Ia in M101, demonstrated that the progenitor did not exceed a radius of 2% solar, fully consistent with the expected white dwarf (Li et al. 2011; Nugent et al. 2011; Bloom et al. 2012). Yet the difficulty and low likelihood of ever directly observing a white dwarf system before it becomes a SN Ia leaves enough uncertainty and model freedom to support the consideration of redshift evolution of the standardized SN Ia luminosity.

From SN Ia observations spanning a wide range of redshifts and sampling the epochs when cosmic expansion accelerates and decelerates, it is possible to distinguish such evolution from the uncertain properties of dark energy (Riess & Livio 2006). As an illustration of the power of SNe Ia at $z > 1$ to separate evolution from cosmology, we briefly reconsider the analysis of Tutusaus et al. (2017), which shows that power-law cosmology, where the scale factor evolves as $a(t) \propto t^n$ for some exponent n , is an equally good fit to SN Ia data (primarily at $z < 1$) as the Λ CDM model (with Ω_m free) when the standardized luminosity is also allowed to vary with redshift according to some simplistic, empirical models of SN Ia evolution. Although such models are not astrophysically motivated, they may be useful for exploring the separation of other SN distance-dependent effects (e.g., gray extinction) from cosmological parameters.

Here, as an illustration, we consider Model B ($\Delta M(z) = \epsilon z^\delta$) from Tutusaus et al. (2017) with fixed $\delta = 0.3$. We separately fit both Λ CDM and power-law cosmology to our combined (Pantheon + MCT) data; in each case, we fit for the Hubble diagram intercept, a cosmological parameter (Ω_m or n), and the amplitude ϵ of the assumed intrinsic luminosity evolution. We compare these fits in Figure 4. Fitting only the SNe at $z < 1$, a power law with $n = 1.1$ is a slightly *better* fit to the SN Ia data than Λ CDM. Indeed, when analyzing the JLA compilation, which features only ~ 5 SNe at $z > 1$, Tutusaus et al. (2017) claims a mild

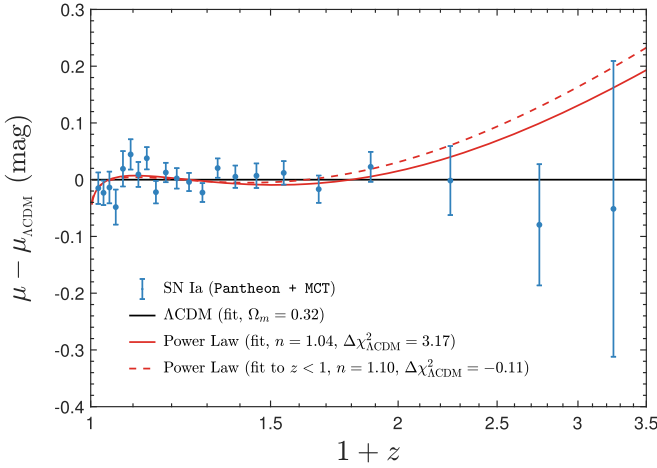


Figure 4. Comparison of Λ CDM and power-law cosmology ($a(t) \propto t^n$) fits to our SN Ia data, where in each case we allow the intrinsic luminosity to evolve as $\Delta M(z) = \epsilon z^\delta$, corresponding to Model B from Tutusaus et al. (2017), where we fix $\delta = 0.3$. The SN data are binned for clarity, and $\Delta\chi^2_{\Lambda\text{CDM}} \equiv \chi^2 - \chi^2_{\Lambda\text{CDM}}$.

preference for the power law (note that their analysis also included BAO and $H(z)$ information).

In contrast, when we include our 24 SNe at $z > 1$, a nearly coasting (marginally accelerating) power-law cosmology (best fit $n = 1.04$) together with simplistic SN Ia evolution is no longer as good a fit as the Λ CDM model, with a relative probability of $\exp(-\Delta\chi^2/2) \approx 20\%$. Without invoking evolution (that is, fixing $\epsilon \equiv 0$), the Λ CDM model is a much better fit than the power-law model, with the latter strongly disfavored with $\Delta\chi^2_{\Lambda\text{CDM}} = 8.3$, a relative probability of 1.6%, when including the new SNe at $z > 1.5$. Meanwhile, assuming Λ CDM and fitting for the evolution amplitude ϵ yields a value consistent with zero, $\epsilon = 0.08 \pm 0.15$, so there is no motivation for including it based on astrophysical *or* empirical considerations. A more comprehensive investigation of SN Ia evolution and cosmology is underway (D. L. Shafer et al., 2018 in preparation).

We note the addition of the MCT SNe to the Pantheon compilation also further reduces the already-low likelihood of the “empty universe” solution where $\Omega_m \approx 0$ and $\Omega_\Lambda \approx 0$ in an open Λ CDM universe, a location Nielsen et al. (2016) claimed to be marginally consistent ($\sim 3\sigma$) with SN data alone using unconventional priors on SN distributions, to the boundary of the 6σ contour.

3.5. $E(z)$ with *WFIRST*

WFIRST was the top space-based recommendation of the 2010 U.S. astronomy and astrophysics decadal survey. The mission is still in formulation, but current plans specify a 2.4 m primary mirror and include a wide-field instrument for cosmology. The cosmology science objectives, as detailed in the most recent report from the Science Definition Team (Spergel et al. 2015), will be accomplished through a combination of SN Ia, galaxy, and weak-lensing surveys.

The *WFIRST* SN survey is anticipated to yield a large sample of thousands of SNe, many at $z > 1$ with precise distances. These SNe will vastly improve upon the high-redshift $E(z)$ measurements available today, allowing nontrivial and

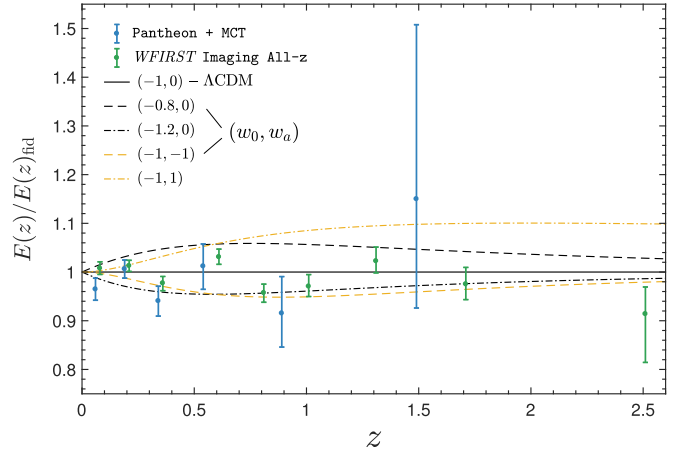


Figure 5. Simulated *WFIRST* constraints on $E(z) \equiv H(z)/H_0$, relative to $E(z)$ for a fiducial Λ CDM model ($\Omega_m = 0.3$). We compare the constraints from current data (blue points) with simulated constraints from the *WFIRST* Imaging All- z observing strategy (green points). We overlay the same dark energy models as in Figure 1.

Table 7
Simulated SN Ia Measurements of $E(z)$ from *WFIRST*

z	$E(z)$ Percent Error ^a
0.07	1.3
0.2	1.1
0.35	1.5
0.6	1.5
0.8	2.0
1.0	2.3
1.3	2.6
1.7	3.4
2.5	8.9

Note.

^a Note that these measurements are not fully independent; there are moderate pairwise correlations among some in the set. They assume a flat universe.

precision tests of the Λ CDM model independent of the BAO and weak-lensing constraints in a redshift range that is currently not well constrained.

Here we wish to forecast realistic constraints on $E(z)$ from *WFIRST*. Typical forecasts (e.g., for dark energy figures of merit) rely on Fisher matrix formalism, which is exact only for Gaussian posterior distributions and otherwise underestimates parameter uncertainties. For SN Ia forecasts, one typically assumes idealized, or roughly estimated, redshift distributions and makes simple assumptions about the measurement error. Here instead we employ a detailed simulation of one potential observing strategy for the *WFIRST* SN survey (Hounsell et al. 2017). We then constrain the $E(z)$ parameters using the methodology of Section 3.2 that was employed in Section 3.3 for our current Pantheon + MCT data.

For our illustration, we consider the Imaging All- z strategy described by Hounsell et al. (2017). This particular strategy relies on multi-band imaging for classification and assumes follow-up spectroscopy will provide host-galaxy redshifts. Hounsell et al. (2017) also assumes a large external sample of 800 SNe at $z < 0.1$. As the size of future systematic

uncertainties is hard to predict, Hounsell et al. (2017) simulates a range of scenarios, and here we opt for all-around optimistic assumptions about future systematic errors (for what this entails, see Hounsell et al. 2017). In this scenario, the contribution of systematic errors is not negligible but is subdominant in the error budget.

In Figure 5, we compare our current Pantheon + MCT constraints on $E(z)$ with simulated constraints from the *WFIRST* Imaging All- z strategy. We find that we are able to constrain $E(z)$ robustly, albeit with moderate pairwise correlations, at 9 redshifts in the range $0.07 < z < 2.5$. In Table 7, we list the percent errors for $E(z)$ corresponding to our forecast. Note that these results are negligibly changed whether we quote percent errors on $E(z)$ or its inverse. We find that *WFIRST* allows 8 measurements of $E(z)$ at the 1%–3% level, along with a robust but less precise measurement at $z \approx 2.5$. Notably, this is a constraint on the expansion rate at a redshift higher than any SN Ia has even been observed to date.

4. Summary and Conclusions

In this study, we analyzed the set of 15 high-redshift SNe Ia from the CANDELS and CLASH *HST* MCT programs, 9 of which ultimately pass classification confidence and quality cuts and 7 of which are at $z > 1.5$ where the relative expansion rate is poorly constrained. These are the first distance estimates for these SNe that are suitable for a joint cosmological analysis with a large compilation of lower-redshift SNe (the Pantheon compilation). We have introduced and employed a procedure to obtain unbiased constraints on the scale-free Hubble parameter $E(z) \equiv H(z)/H_0$ using only this extended Pantheon + MCT sample of SNe Ia (Table 6, Figures 1–2). The CANDELS and CLASH SNe at $z \gtrsim 1.5$ extend the Hubble diagram and allow us to achieve a robust measurement of the expansion rate at $z = 1.5$ that efficiently summarizes the cosmological leverage of these new SNe. Our measurement of $E(z = 1.5)^{-1} = 0.337 \pm 0.078$ (equivalently, $E(z = 1.5) = 2.69^{+0.86}_{-0.52}$) assumes a flat universe and smooth expansion history but is otherwise model-independent.

We also have demonstrated that the set of $E(z)$ measurements can serve as a form of SN Ia data compression, allowing us to summarize SN Ia constraints on spatially flat cosmological models that feature a smooth expansion history, which comprise the majority of the commonly studied dark energy models. The $E(z)$ are very economical, accurately reproducing parameter posteriors (even when non-Gaussian) using just 6 measured quantities in place of >1000 (Figure 3). The computation time for this $E(z)$ likelihood, relative to that for the full SN Ia likelihood, is negligible.

Future large, high-quality samples of high-redshift SNe Ia, notably from *WFIRST*, will allow precision constraints on the dark energy equation-of-state parameter w , especially for dynamical dark energy featuring a time-varying value of w . Still, there are uses for such high-redshift SNe beyond direct dark energy constraints, inspiring us to perform two additional investigations.

First, using our combined Pantheon + MCT set of SNe Ia, we have briefly illustrated how the added leverage of our larger sample of SNe at $z > 1$, including 7 at $z > 1.5$, can help distinguish empirical SN Ia evolution and nonstandard cosmological models from the Λ CDM model (Figure 4). We have shown that, while a nearly coasting power-law model

($a(t) \propto t^n$ with $n \approx 1$) is as good a fit to the $z < 1$ data as Λ CDM (at least when certain forms of SN evolution are allowed), adding the $z > 1$ SNe disfavors the power law, indicating a relative probability of $\sim 20\%$, even when permitting the same SN evolution.

Second, we have used our $E(z)$ procedure in conjunction with a realistic simulation of a potential *WFIRST* SN Ia observing strategy to forecast optimistic *WFIRST* constraints on $E(z)$. We find that *WFIRST* will permit 8 measurements of $E(z)$ at the 1%–3% level across a wide range of redshifts, along with a robust measurement at $z \approx 2.5$ (Figure 5, Table 7). Such measurements will constitute precise tests of our expectations from the Λ CDM model separately from BAO and other high-redshift distance probes.

We thank Rebekah Hounsell for providing the *WFIRST* SN Ia simulations and the anonymous referee for helpful comments. It is our pleasure to thank program coordinators Patricia Royle and Beth Perriello, as well as the entire Space Telescope Science Institute (STScI) scheduling team, for their tireless efforts that made the CANDELS survey and the SN follow-up program possible.

This work was principally based on observations made with the NASA/ESA *Hubble Space Telescope*, which is operated by the Association of Universities for Research in Astronomy (AURA), Inc., under NASA contract NAS5-26555. These observations are associated with program IDs 12060, 12061, 12062, 12442, 12443, 12444, 12445, 12099, 12461, and 13063. The analysis presented here made extensive use of the Mikulski Archive for Space Telescopes (MAST). STScI is operated by AURA, Inc., under NASA contract NAS5-26555. Support for MAST for non-*HST* data is provided by the NASA Office of Space Science via grant NNX13AC07G and by other grants and contracts. Some of the data presented herein were obtained at the W.M. Keck Observatory, which is operated as a scientific partnership among the California Institute of Technology, the University of California, and NASA; the Observatory was made possible by the generous financial support of the W.M. Keck Foundation.

Financial support was broadly provided by NASA through grants HST-GO-12060 and HST-GO-12099 from STScI, and to SAR through grant HST-HF-51312. AVF is also grateful for generous financial assistance from the Christopher R. Redlich Fund, the TABASGO Foundation, and the Miller Institute for Basic Research in Science (U.C. Berkeley). AM acknowledges the financial support of the Brazilian funding agency FAPESP (Postdoc fellowship, process number 2014/11806-9). OG is supported by an NSF Astronomy and Astrophysics Postdoctoral Fellowship under award AST-1602595. JH was supported by a VILLUM FONDEN Investigator grant (project number 16599). SJ was supported by JPL RSAs 143563, 1448524, 1460278, and 1473597.

Facility: *HST* (WFC3).

Appendix CANDELS + CLASH Light-Curve Photometry

The light-curve photometry for the 15 likely SNe Ia is given in Table 8.

Table 8
CANDELS + CLASH Light-curve Photometry

MJD	Filter	Band	Flux ^a	Flux Unc.	Mag ^b	Mag Unc.
SN CLA10Cal (Caligula)						
55599.42	F814W	I	11.982	1.084	24.8	0.1
55538.409	F125W	J	−0.035	0.847	>26.5	...
55558.446	F125W	J	1.359	0.596	>26.9	...
55579.348	F125W	J	0.805	0.637	>26.8	...
55599.383	F125W	J	0.791	0.77	>26.6	...
55538.418	F160W	H	0.794	0.797	>26.6	...
55558.455	F160W	H	0.412	1.265	>26.1	...
55579.357	F160W	H	0.612	1.175	>26.1	...
55599.392	F160W	H	0.397	2.311	>25.4	...
55613.163	F160W	H	1.386	0.775	>26.6	...
SN CLF11Ves (Vespasian)						
55715.81	F775W	X	0.916	1.056	>26.2	...
55736.78	F775W	X	10.157	1.05	24.98	0.11
55747.67	F775W	X	8.074	0.97	25.23	0.13
55715.8	F850LP	Z	2.228	0.976	>26.3	...
55736.77	F850LP	Z	14.909	0.96	24.57	0.07
55746.82	F850LP	Z	11.119	1.252	24.88	0.12
55762.2	F850LP	Z	7.178	0.972	25.36	0.15
55776.58	F850LP	Z	3.46	0.937	26.15	0.29
SN CLH11Tra (Trajan)						
55833.68	F775W	X	0.321	0.947	>26.4	...
55854.04	F775W	X	5.673	1.576	25.62	0.3
55872.41	F775W	X	6.192	1.022	25.52	0.18
55885.16	F775W	X	2.68	0.983	>26.3	...
55833.67	F850LP	Z	−0.348	0.778	>26.6	...
55872.443	F125W	J	13.465	1.011	24.68	0.08
55885.216	F125W	J	8.339	0.999	25.2	0.12
55872.45	F160W	H	12.796	1.416	24.73	0.11
55885.224	F160W	H	8.097	1.191	25.23	0.15
SN CLP12Get (Geta)						
56048.121	F125W	J	−0.073	0.575	>26.9	...
56078.249	F125W	J	0.253	0.938	>26.4	...
56105.648	F125W	J	3.516	1.104	26.13	0.31
56117.553	F125W	J	6.741	1.124	25.43	0.17
56131.585	F125W	J	10.363	1.234	24.96	0.12
56138.833	F125W	J	10.624	1.153	24.93	0.11
56146.219	F125W	J	12.151	1.225	24.79	0.1
56164.368	F125W	J	8.263	1.215	25.21	0.15
56184.516	F125W	J	4.321	1.071	25.91	0.25
56197.283	F125W	J	3.601	1.186	26.11	0.33
56048.129	F160W	H	1.058	1.65	>25.8	...
56078.257	F160W	H	0.899	1.588	>25.8	...
56105.656	F160W	H	2.499	0.937	>26.4	...
56117.561	F160W	H	6.284	1.077	25.5	0.17
56131.591	F160W	H	9.995	1.238	25.0	0.12
56138.839	F160W	H	10.703	1.291	24.93	0.12
56146.227	F160W	H	8.411	1.253	25.19	0.15
56164.376	F160W	H	6.156	1.265	25.53	0.21
56184.524	F160W	H	4.135	1.02	25.96	0.25
56197.291	F160W	H	5.663	1.278	25.62	0.23
SN COS12Car (Carter)						
55954.58	F606W	V	0.195	0.126	>28.6	...
55967.35	F850LP	Z	0.988	0.597	>26.9	...
55908.8	F125W	J	2.037	0.478	26.73	0.23
55957.504	F125W	J	7.909	0.578	25.25	0.07
55967.543	F125W	J	6.309	0.684	25.5	0.11
55968.674	F125W	J	5.923	0.851	25.57	0.14

Table 8
(Continued)

MJD	Filter	Band	Flux ^a	Flux Unc.	Mag ^b	Mag Unc.
55977.603	F125W	J	6.116	0.537	25.53	0.09
55991.105	F125W	J	3.063	0.521	26.28	0.17
56006.455	F125W	J	3.003	0.4	26.31	0.13
56026.291	F125W	J	1.335	0.335	27.19	0.25
55908.806	F160W	H	2.256	0.539	26.62	0.24
55957.516	F160W	H	7.088	0.601	25.37	0.08
55963.439	F160W	H	6.32	0.758	25.5	0.12
55977.588	F160W	H	4.707	0.739	25.82	0.16
55991.09	F160W	H	5.313	0.756	25.69	0.14
56006.389	F160W	H	4.784	0.531	25.8	0.11
56026.216	F160W	H	4.259	0.518	25.93	0.12
SN EGS11Oba (Obama)						
55659.793	F125W	J	0.782	0.636	>26.8	...
55710.639	F125W	J	7.038	0.764	25.38	0.11
55725.214	F125W	J	7.377	0.758	25.33	0.1
55739.126	F125W	J	4.125	0.691	25.96	0.17
55753.522	F125W	J	3.757	0.715	26.06	0.19
55659.799	F160W	H	0.724	0.646	>26.8	...
55710.645	F160W	H	6.529	0.713	25.46	0.11
55725.221	F160W	H	6.968	0.845	25.39	0.12
55739.118	F160W	H	4.252	0.712	25.93	0.17
55753.647	F160W	H	4.585	0.707	25.85	0.15
SN EGS13Rut (Rutledge)						
56438.18	F606W	V	−0.04	0.103	>28.8	...
56438.24	F814W	I	1.684	0.389	26.93	0.25
56447.42	F814W	I	2.228	0.384	26.63	0.19
56437.624	F125W	J	7.044	0.732	25.38	0.1
56447.139	F125W	J	8.717	0.751	25.15	0.09
56460.64	F125W	J	8.766	0.696	25.14	0.08
56482.351	F125W	J	6.659	0.669	25.44	0.1
56437.631	F160W	H	6.361	0.673	25.49	0.11
56447.253	F160W	H	7.588	0.747	25.3	0.1
56460.647	F160W	H	9.158	0.832	25.1	0.09
56482.359	F160W	H	6.599	0.705	25.45	0.11
56501.147	F160W	H	4.986	0.674	25.76	0.14
56522.425	F160W	H	3.93	0.645	26.01	0.16
SN GND12Col (Colfax)						
56069.98	F606W	V	−0.269	0.285	>27.7	...
56016.29	F814W	I	0.192	0.24	>27.9	...
56074.61	F814W	I	0.003	0.317	>27.6	...
56116.49	F814W	I	−0.071	0.096	>28.9	...
56128.42	F814W	I	−0.207	0.108	>28.7	...
56180.92	F814W	I	0.166	0.154	>28.3	...
56186.47	F814W	I	−0.191	0.119	>28.6	...
56200.16	F814W	I	−0.105	0.129	>28.5	...
56152.07	F850LP	Z	0.043	0.323	>27.5	...
56018.628	F125W	J	−0.016	0.226	>27.9	...
56074.305	F125W	J	3.877	0.464	26.03	0.12
56084.685	F125W	J	3.609	0.479	26.11	0.13
56103.172	F125W	J	2.818	0.488	26.38	0.17
56129.454	F125W	J	0.858	0.319	>27.5	...
56145.532	F125W	J	0.715	0.333	>27.5	...
56183.129	F125W	J	−0.011	0.228	>27.9	...
56241.974	F125W	J	0.0	0.246	>27.8	...
56297.69	F125W	J	0.045	0.239	>27.9	...
56084.763	F127M	O	5.363	0.623	25.68	0.12
56082.777	F139M	P	5.61	0.852	25.63	0.15
56083.095	F140W	N	5.085	0.485	25.73	0.1
56091.533	F140W	N	4.863	0.748	25.78	0.15
56104.231	F140W	N	3.548	0.785	26.12	0.22

Table 8
(Continued)

MJD	Filter	Band	Flux ^a	Flux Unc.	Mag ^b	Mag Unc.
56085.627	F153M	Q	4.825	0.891	25.79	0.18
56018.635	F160W	H	-0.048	0.763	>26.6	...
56074.312	F160W	H	5.735	0.723	25.6	0.13
56084.645	F160W	H	4.242	0.647	25.93	0.15
56103.164	F160W	H	3.769	0.649	26.06	0.17
56129.379	F160W	H	1.694	0.515	26.93	0.3
56145.47	F160W	H	2.391	0.628	26.55	0.26
56183.136	F160W	H	1.177	0.623	>26.8	...
56241.981	F160W	H	0.278	1.21	>26.1	...
56297.697	F160W	H	-0.098	0.922	>26.4	...
SN GND13Cam (Camille)						
56356.28	F814W	I	5.791	0.456	25.59	0.08
56391.79	F814W	I	0.558	0.353	>27.4	...
56356.43	F814W	I	8.852	1.719	25.13	0.21
56236.854	F125W	J	0.0	0.119	>28.6	...
56296.624	F125W	J	0.507	0.208	>28.0	...
56346.757	F125W	J	4.808	0.302	25.8	0.06
56369.646	F125W	J	6.461	0.32	25.47	0.05
56382.019	F125W	J	5.118	0.298	25.73	0.06
56406.455	F125W	J	2.898	0.247	26.34	0.09
56425.556	F125W	J	1.334	0.284	27.19	0.21
56459.362	F125W	J	0.604	0.234	>27.9	...
56514.194	F125W	J	0.746	0.263	>27.8	...
56356.545	F140W	N	6.401	0.524	25.48	0.08
56236.861	F160W	H	0.243	0.286	>27.7	...
56296.633	F160W	H	0.437	0.324	>27.5	...
56346.764	F160W	H	4.367	0.417	25.9	0.1
56369.638	F160W	H	4.734	0.39	25.81	0.08
56382.011	F160W	H	3.097	0.371	26.27	0.12
56406.462	F160W	H	2.323	0.336	26.59	0.14
56425.548	F160W	H	2.295	0.37	26.6	0.16
56459.369	F160W	H	1.082	0.359	27.41	0.33
56514.201	F160W	H	0.416	0.307	>27.6	...
SN GND13Gar (Garner)						
56577.2	F814W	I	0.739	0.44	>27.2	...
56446.46	F850LP	Z	5.836	0.844	25.58	0.16
56347.887	F125W	J	0.177	0.304	>27.6	...
56406.654	F125W	J	11.106	0.523	24.89	0.05
56425.671	F125W	J	16.562	0.627	24.45	0.04
56459.229	F125W	J	7.356	0.499	25.33	0.07
56467.226	F125W	J	8.3	0.605	25.2	0.07
56511.203	F125W	J	3.154	0.499	26.25	0.16
56347.895	F160W	H	-0.058	0.888	>26.4	...
56406.661	F160W	H	6.989	0.717	25.39	0.1
56425.664	F160W	H	8.138	0.73	25.22	0.09
56459.236	F160W	H	5.696	0.656	25.61	0.12
56467.22	F160W	H	6.386	0.846	25.49	0.13
56511.21	F160W	H	1.843	0.625	>26.8	...
SN GND13Jay (Jay)						
56446.46	F850LP	Z	5.459	1.013	25.66	0.2
56391.73	F814W	I	1.39	0.222	27.14	0.17
56577.2	F814W	I	0.305	0.458	>27.2	...
56347.887	F125W	J	0.138	0.267	>27.7	...
56406.654	F125W	J	12.196	0.555	24.78	0.05
56425.671	F125W	J	11.243	0.576	24.87	0.05
56459.229	F125W	J	5.738	0.484	25.6	0.08
56467.226	F125W	J	5.179	0.538	25.71	0.1
56511.203	F125W	J	2.185	0.469	26.65	0.21
56347.895	F160W	H	0.0	0.669	>26.7	...

Table 8
(Continued)

MJD	Filter	Band	Flux ^a	Flux Unc.	Mag ^b	Mag Unc.
56406.661	F160W	H	9.322	0.748	25.08	0.08
56425.664	F160W	H	6.675	0.756	25.44	0.11
56459.236	F160W	H	5.514	0.609	25.65	0.11
56467.22	F160W	H	5.071	0.724	25.74	0.14
56511.21	F160W	H	2.77	0.641	26.39	0.23
SN GND13Sto (Stone)						
56458.33	F814W	I	0.632	0.366	>27.4	...
56403.398	F125W	J	0.785	0.372	>27.4	...
56457.501	F125W	J	3.587	0.504	26.11	0.14
56467.888	F125W	J	6.815	0.52	25.42	0.08
56490.59	F125W	J	7.489	0.614	25.31	0.08
56513.396	F125W	J	4.06	0.532	25.98	0.13
56531.078	F125W	J	1.599	0.614	>26.8	...
56474.38	F139M	P	6.79	1.279	25.42	0.19
56474.51	F140W	N	7.239	0.817	25.35	0.11
56474.912	F153M	Q	6.733	1.018	25.43	0.15
56403.405	F160W	H	0.685	0.625	>26.8	...
56457.508	F160W	H	4.431	0.674	25.88	0.15
56467.896	F160W	H	5.174	0.646	25.72	0.12
56474.519	F160W	H	8.116	0.628	25.23	0.08
56490.584	F160W	H	6.292	0.723	25.5	0.11
56513.404	F160W	H	5.539	0.728	25.64	0.13
56531.057	F160W	H	3.829	0.681	26.04	0.18
56551.177	F160W	H	2.981	0.534	26.31	0.18
SN GSD10Pri (Primo)						
55607.39	F814W	I	-0.148	0.911	>26.4	...
55620.78	F814W	I	0.054	0.367	>27.4	...
55626.45	F814W	I	-0.393	0.36	>27.4	...
55647.07	F814W	I	-0.438	0.262	>27.8	...
55584.58	F850LP	Z	-1.143	0.534	>27.0	...
55598.62	F850LP	Z	1.54	0.597	>26.9	...
55620.18	F850LP	Z	0.147	0.495	>27.1	...
55412.131	F125W	J	0.138	0.069	>29.2	...
55417.79	F125W	J	0.027	0.063	>29.3	...
55423.131	F125W	J	0.17	0.114	>28.7	...
55479.905	F125W	J	9.27	0.627	25.08	0.07
55501.266	F125W	J	8.604	0.879	25.16	0.1
55507.662	F125W	J	6.66	0.423	25.44	0.06
55521.198	F125W	J	4.387	0.421	25.89	0.1
55528.374	F125W	J	4.437	0.546	25.88	0.12
55535.157	F125W	J	2.875	0.33	26.35	0.11
55543.739	F125W	J	1.891	0.243	26.81	0.13
55578.695	F125W	J	1.205	0.424	>27.2	...
55625.62	F125W	J	0.909	0.448	>27.2	...
55718.133	F125W	J	-0.014	0.19	>28.1	...
55818.755	F125W	J	0.162	0.195	>28.1	...
55974.319	F125W	J	0.029	0.244	>27.8	...
55415.859	F160W	H	0.0	0.098	>28.8	...
55416.858	F160W	H	0.0	0.071	>29.2	...
55424.047	F160W	H	0.156	0.115	>28.7	...
55438.906	F160W	H	0.198	0.111	>28.7	...
55453.798	F160W	H	2.024	0.256	26.73	0.13
55479.899	F160W	H	8.43	0.707	25.19	0.08
55494.169	F160W	H	6.721	0.59	25.43	0.09
55507.679	F160W	H	6.12	0.601	25.53	0.1
55522.904	F160W	H	5.249	0.805	25.7	0.15
55528.367	F160W	H	4.76	0.752	25.81	0.16
55535.291	F160W	H	3.281	0.464	26.21	0.14
55578.687	F160W	H	1.477	0.55	>27.0	...
55625.613	F160W	H	0.474	0.663	>26.8	...

Table 8
(Continued)

MJD	Filter	Band	Flux ^a	Flux Unc.	Mag ^b	Mag Unc.
SN GSD11Was (Washington)						
55621.05	F814W	I	8.785	0.392	25.14	0.05
55647.34	F814W	I	3.344	0.287	26.19	0.09
55656.4	F814W	I	2.276	0.373	26.61	0.18
55576.43	F125W	J	−0.013	0.343	>27.5	...
55625.085	F125W	J	12.234	0.616	24.78	0.05
55635.536	F125W	J	10.003	0.515	25.0	0.05
55647.127	F125W	J	7.605	0.572	25.3	0.08
55656.45	F125W	J	6.862	0.634	25.41	0.09
55720.129	F125W	J	1.122	0.552	>27.0	...
55770.903	F125W	J	1.783	0.506	26.87	0.28
55816.692	F125W	J	0.037	0.62	>26.8	...
55576.422	F160W	H	−0.061	0.832	>26.5	...
55625.077	F160W	H	11.116	0.753	24.89	0.07
55635.338	F160W	H	7.612	0.717	25.3	0.09
55647.119	F160W	H	7.493	0.828	25.31	0.11
55656.442	F160W	H	4.581	0.694	25.85	0.15
55720.122	F160W	H	3.18	0.775	26.24	0.24
55770.91	F160W	H	1.361	0.679	>26.7	...
55816.699	F160W	H	0.0	0.737	>26.6	...
SN UDS10Wil (Wilson)						
55558.33	F814W	I	−0.146	0.176	>28.2	...
55574.65	F850LP	Z	−0.019	0.502	>27.1	...
55511.201	F125W	J	2.193	0.511	26.65	0.23
55560.786	F125W	J	5.182	0.565	25.71	0.11
55573.221	F125W	J	2.806	0.399	26.38	0.14
55584.405	F125W	J	1.831	0.364	26.84	0.2
55596.135	F125W	J	1.451	0.368	27.1	0.25
55608.24	F125W	J	0.698	0.297	>27.6	...
55511.181	F160W	H	2.724	0.566	26.41	0.21
55560.721	F160W	H	5.901	0.652	25.57	0.11
55572.954	F160W	H	4.729	0.592	25.81	0.13
55584.343	F160W	H	4.19	0.545	25.94	0.13
55596.06	F160W	H	2.964	0.566	26.32	0.19
55608.106	F160W	H	1.419	0.498	>27.1	...

Notes.

^a Flux density in FLUXCAL units used by SNANA, which are normalized to a zeropoint of 27.5.

^b Magnitudes are on the AB photometric system. For epochs where the measured flux is $<3\sigma$ significance, we report the magnitude as a 3σ upper limit.

ORCID iDs

Steven A. Rodney <https://orcid.org/0000-0003-1947-687X>
 Henry C. Ferguson <https://orcid.org/0000-0001-7113-2738>
 Marc Postman <https://orcid.org/0000-0002-9365-7989>
 Or Graur <https://orcid.org/0000-0002-4391-6137>
 Saurabh W. Jha <https://orcid.org/0000-0001-8738-6011>
 Brian Hayden <https://orcid.org/0000-0001-9200-8699>
 Alberto Molino <https://orcid.org/0000-0002-5007-680X>
 Jens Hjorth <https://orcid.org/0000-0002-4571-2306>
 Peter M. Garnavich <https://orcid.org/0000-0003-4069-2817>
 David O. Jones <https://orcid.org/0000-0002-6230-0151>
 Anton M. Koekemoer <https://orcid.org/0000-0002-6610-2048>
 Norman A. Grogin <https://orcid.org/0000-0001-9440-8872>
 Gabriel Brammer <https://orcid.org/0000-0003-2680-005X>

Shoubaneh Hemmati <https://orcid.org/0000-0003-2226-5395>

Schuyler Wolff <https://orcid.org/0000-0002-9977-8255>

Alexei V. Filippenko <https://orcid.org/0000-0003-3460-0103>

Hooshang Nayyeri <https://orcid.org/0000-0001-8242-9983>

U Vivian <https://orcid.org/0000-0002-1912-0024>

David C. Koo <https://orcid.org/0000-0003-3385-6799>

Larry Bradley <https://orcid.org/0000-0002-7908-9284>

Dan Coe <https://orcid.org/0000-0001-7410-7669>

References

- Ade, P. A. R., Aghanim, N., Arnaud, M., et al. 2016, *A&A*, 594, A13
 Alam, S., Ata, M., Bailey, S., et al. 2017, *MNRAS*, 470, 2617
 Andersen, P., & Hjorth, J. 2017, *MNRAS*, 472, 1413
 Arnett, W. D. 1969, *ApJ*, 157, 1369
 Arnett, W. D., Branch, D., & Wheeler, J. C. 1985, *Natur*, 314, 337
 Avgoustidis, A., Verde, L., & Jimenez, R. 2009, *JCAP*, 0906, 012
 Barbary, K., Aldering, G., Amanullah, R., et al. 2012, *ApJ*, 745, 32
 Betoule, M., Kessler, R., Guy, J., et al. 2014, *A&A*, 568, A22
 Bloom, J. S., Kasen, D., Shen, K., et al. 2012, *ApJL*, 744, L17
 Chevallier, M., & Polarski, D. 2001, *IMPD*, 10, 213
 Colgate, S. A., & McKee, C. 1969, *ApJ*, 157, 623
 Conley, A., Guy, J., Sullivan, M., et al. 2011, *ApJS*, 192, 1
 Daly, R. A., & Djorgovski, S. G. 2003, *ApJ*, 597, 9
 Daly, R. A., & Djorgovski, S. G. 2004, *ApJ*, 612, 652
 Daly, R. A., Djorgovski, S. G., Freeman, K. A., et al. 2008, *ApJ*, 677, 1
 Dawson, K. S., Aldering, G., Amanullah, R., et al. 2009, *AJ*, 138, 1271
 Dickinson, M., Papovich, C., & Ferguson, H. C. 2001, in *Deep Fields*, ed. S. Cristiani, A. Renzini, & R. E. Williams (Berlin: Springer), 68
 Frederiksen, T. F., Hjorth, J., Maund, J. R., et al. 2012, *ApJ*, 760, 125
 Giavalisco, M., Ferguson, H. C., Koekemoer, A. M., et al. 2004, *ApJL*, 600, L93
 Gilliland, R. L., Nugent, P. E., & Phillips, M. M. 1999, *ApJ*, 521, 30
 Graur, O., Rodney, S. A., Maoz, D., et al. 2014, *ApJ*, 783, 28
 Grogin, N. A., Kocevski, D. D., Faber, S. M., et al. 2011, *ApJS*, 197, 35
 Guy, J., Astier, P., Baumont, S., et al. 2007, *A&A*, 466, 11
 Hicken, M., Challis, P., Jha, S., et al. 2009, *ApJ*, 700, 331
 Hounsell, R., Scolnic, D., Foley, R. J., et al. 2017, arXiv:1702.01747
 Hoyle, F., & Fowler, W. A. 1960, *ApJ*, 132, 565 [Erratum: *ApJ*, 134, 1028 (1961)]
 Ishida, E. E. O., & de Souza, R. S. 2011, *A&A*, 527, A49
 Jones, D. O., Rodney, S. A., Riess, A. G., et al. 2013, *ApJ*, 768, 166
 Jönsson, J., Dahlén, T., Goobar, A., et al. 2006, *ApJ*, 639, 991
 Jönsson, J., Sullivan, M., Hook, I., et al. 2010, *MNRAS*, 405, 535
 Kahaner, D., Moler, C., & Nash, S. 1988, *Numerical Methods and Software* (Upper Saddle River, NJ: Prentice-Hall)
 Kessler, R., Becker, A. C., Cinabro, D., et al. 2009, *ApJS*, 185, 32
 Kessler, R., & Scolnic, D. 2017, *ApJ*, 836, 56
 Koekemoer, A. M., Faber, S. M., Ferguson, H. C., et al. 2011, *ApJS*, 197, 36
 Li, W., Bloom, J. S., Podsiadlowski, P., et al. 2011, *Natur*, 480, 348
 Linder, E. V. 2003, *PhRvL*, 90, 091301
 Mortonson, M. J., Hu, W., & Huterer, D. 2009, *PhRvD*, 79, 023004
 Mortonson, M. J., Hu, W., & Huterer, D. 2010, *PhRvD*, 81, 063007
 Mortsell, E., & Clarkson, C. 2009, *JCAP*, 0901, 044
 Nielsen, J. T., Guffanti, A., & Sarkar, S. 2016, *Sci. Rep.*, 6, 35596
 Nomoto, K., Thielemann, F. K., & Yokoi, K. 1984, *ApJ*, 286, 644
 Nugent, P. E., Sullivan, M., Cenko, S. B., et al. 2011, *Natur*, 480, 344
 Postman, M., Coe, D., Benítez, N., et al. 2012, *ApJS*, 199, 25
 Rest, A., Scolnic, D., Foley, R. J., et al. 2014, *ApJ*, 795, 44
 Riess, A. G., & Livio, M. 2006, *ApJ*, 648, 884
 Riess, A. G., Macri, L. M., Hoffmann, S. L., et al. 2016, *ApJ*, 826, 56
 Riess, A. G., Nugent, P. E., Gilliland, R. L., et al. 2001, *ApJ*, 560, 49
 Riess, A. G., Press, W. H., & Kirshner, R. P. 1996, *ApJ*, 473, 88
 Riess, A. G., Strolger, L.-G., Casertano, S., et al. 2007, *ApJ*, 659, 98
 Riess, A. G., Strolger, L.-G., Tonry, J., et al. 2004, *ApJ*, 607, 665
 Rodney, S. A., Riess, A. G., Dahlen, T., et al. 2012, *ApJ*, 746, 5
 Rodney, S. A., Riess, A. G., Scolnic, D. M., et al. 2015, *AJ*, 150, 156
 Rodney, S. A., Riess, A. G., Strolger, L.-G., et al. 2014, *AJ*, 148, 13
 Rubin, D., Knop, R. A., Rykoff, E., et al. 2013, *ApJ*, 763, 35
 Sahni, V., & Starobinsky, A. 2006, *IMPD*, 15, 2105

- Scolnic, D., Casertano, S., Riess, A. G., et al. 2015, [ApJ](#), **815**, 117
- Scolnic, D., & Kessler, R. 2016, [ApJL](#), **822**, L35
- Scolnic, D., Rest, A., Riess, A. G., et al. 2014, [ApJ](#), **795**, 45
- Scolnic, D. M., Jones, D. O., Rest, A., et al. 2017, arXiv:[1710.00845](#)
- Shafieloo, A. 2007, [MNRAS](#), **380**, 1573
- Shafieloo, A., Alam, U., Sahni, V., & Starobinsky, A. A. 2006, [MNRAS](#), **366**, 1081
- Shafieloo, A., & Clarkson, C. 2010, [PhRvD](#), **81**, 083537
- Spergel, D., Gehrels, N., Baltay, C., et al. 2015, arXiv:[1503.03757](#)
- Stritzinger, M. D., Phillips, M. M., Boldt, L. N., et al. 2011, [AJ](#), **142**, 156
- Strolger, L.-G., Riess, A. G., Dahlen, T., et al. 2004, [ApJ](#), **613**, 200
- Suzuki, N., Rubin, D., Lidman, C., et al. 2012, [ApJ](#), **746**, 85
- Tegmark, M. 2002, [PhRvD](#), **66**, 103507
- Tutusaus, I., Lamine, B., Dupays, A., & Blanchard, A. 2017, [A&A](#), **602**, A73
- Wang, Y., & Tegmark, M. 2005, [PhRvD](#), **71**, 103513